STM JOURNALS

Journal of
Polymer & Composites

ISSN: 2321-2810 (Online)
ISSN: 2321-8525 (Print)
Volume 13, Special Issue 4, 2025
DOI (Journal): 10.37591/JoPC

https://journals.stmjournals.com/jopc

Review JoPC

Improved Photocatalytic Activity for Removal of Methylene Blue Dye from Aqueous Solutions with La_2O_3-Modified Ceria Heterostructured Binary Oxide Nanocomposite Particles

Atikur Rahman [1,*], Manoj Kumar [2]

Abstract

The current study aimed to examine the photocatalytic efficacy of a bimetallic CeO_2-La_2O_3 hetero-NC in comparison to monometallic CeO_2 and La_2O_3 nanoparticles (NPs), utilizing Methylene Blue (MB)as pollutant sample under natural solar and UVirradiation. The coprecipitation method was utilized to produce a bimetallic CeO_2-La_2O_3 hetero-NC. Following this, the nanostructures underwent characterization through various techniques including FT-IR, FE-SEM, XRD, UV Vis- DRS, Raman, and Photoluminescence spectroscopy. The catalytic activity of the bimetallic CeO_2-La_2O_3 hetero-NC is superior and follows pseudo-first-order kinetics. In addition, the photocatalytic mechanism has been briefly explained. The bimetallic CeO_2-La_2O_3 hetero-NC exhibits higher photocatalytic activity 93% against MB than pure CeO_2 and La_2O_3 due to the formation of p-n heterostructures. In 100 min under UV conditions, CeO_2 degraded 78% of MB, while La_2O_3 only degraded 58%. Similarly, under solar irradiation, CeO_2-La_2O_3 NC demonstrated 96% effectiveness in 180 minutes when compared to pure metal oxide nanoparticles. The findings suggest that the bimetallic CeO_2-La_2O_3 hetero-NC has desirable structural and optical properties, making it a promising material for optoelectronic and photocatalytic applications.

Graphical Abstract

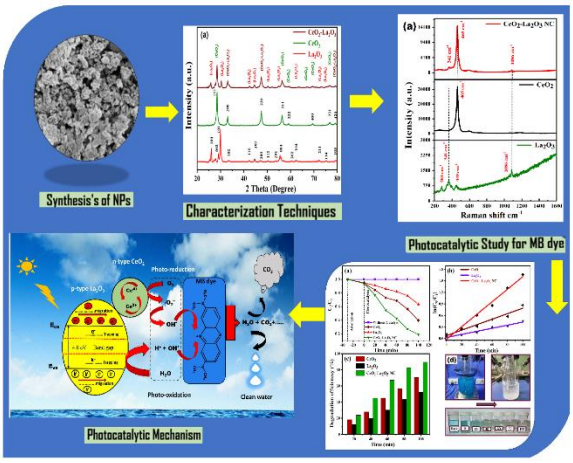

***Author for Correspondence**
Atikur Rahman

[1]Professor, Department of Metallurgical and Materials Engineering, National Institute of Technology, Hazratbal, Srinagar, Jammu and Kashmir, India
[2] Research Scholar, Department of Metallurgical and Materials Engineering, National Institute of Technology, Hazratbal, Srinagar, Jammu and Kashmir, India

Received Date: November 12, 2024
Accepted Date: June 02, 2025
Published Date: June 15, 2025

Citation: Atikur Rahman, Manoj Kumar. Improved Photocatalytic Activity for Removal of Methylene Blue Dye from Aqueous Solutions with La_2O_3-Modified Ceria Heterostructured Binary Oxide Nanocomposite Particles. Journal of Polymer & Composites. 2025; 13(Special Issue 4): S514–S532p.

Keywords: Wastewater treatment,Oxide NPs, bimetallic heterocomposites, characterization studies, p-n heterojunction, photocatalytic activities

INTRODUCTION

Groundwater, surface water, sewage, and drinking water all contain a variety of organic pollutants, making them a key source of concern

[1]. Polluted wastewater from businesses such as fabrication, textiles, insecticides, and medicines is a major global public health concern[2].Organic dyes are a safer alternative to the harmful chemicals used in traditional dyeing, and they are commonlyemployed in the fabric stuff, food products, furniture, and varnish segments[3]. However, discharging dye-contaminated wastewater carries considerable environmental as well as health risks[4]. Dye-contaminated wastewater impacts aquatic ecosystems by reducing sunlight penetration, interfering with photosynthesis, and reducing oxygen generation, all of which have an impact on dependent organisms[5]. Reduced oxygen levels endanger the survival of fish and other aquatic life, prompting international efforts to find environmentally friendly and health-conscious ways to clean dye-contaminated wastewater[6]. Numerous wastewater managementtechnologies have been described, together with chemical treatment, filtration, boiling, reverse osmosis, chlorination, advanced oxidation processes (AOPs), and distillation[6-8]. Among various technologies, photocatalysis has received a lot of attention for its potential in environmental remediation and energy generation. This innovative photooxidation technology is an effective way to remove dangerous pollutants and toxins from wastewater[9]. Semiconductor based catalysts for effluent purification and environmental remediation have received recent attention due to their efficient use of solar energy, a natural and environmentally friendly resource. These photocatalyst materials are widely used worldwide[10]. Metal oxide nanoparticles (MONPs) have received substantial interest in photocatalysis due to their probable in environmental remediation and energy regeneration[11]. MOare ionic compounds composed of completely charged metal ions and negatively charged O_2ions bound together by strong ionic interactions[12]. Over the last decade, researchers have investigated rare earth metals having 1-100 nanostructures. Because of the electrons in the 4f orbital, and these elements have distinct features and tremendous potential in a variety of scientific and energy disciplines[13]. The correlation between particle size and electron configuration in MOis well established. As particle size decreases, band gaps and excited energy levels alter dramatically[14]. The utilization of hybrid semiconductor materials, which are created by combining p-n-type linked heterostructures, is an efficient way to eliminate organic contaminants from wastewater[15]. Mainconditions for developing p-n heterojunctions in oxide composites for practical applications include material selectivity, a suitable band structure, and energy band gap edges[15]. Cerium, the first rare earth lanthanide discovered as nanoparticles, forms fluorite with oxygen[16]. CeO_2, acting as an antioxidant by cycling between 3^+ and 4^+ states, is valuable as a fuel cell electrolyte[17]. It is also researched in nanotechnology for fuel additives, catalytic converters, and self-repairing antioxidants[18].Lanthanum oxide, a crucial p-type semiconductor in rare earth metals[19], having application in laser communications, solar cells[20], and photocatalysis[21]. It is essential in electrochemistry for sustainably generated catalysts and can also function as electrodes[22].Thesematerials are developed through different process such as: chemical procedures (e.g., sol-gel, hydrothermal, vapor deposition) and physical approaches (e.g., flame spray, milling, laser ablation)[23].This study aims to develop enhanced photocatalyst materials for efficient solar energy utilization, particularly in dye degradation. The design and synthesis of a p–n heterojunction catalyst offer the potential to improve photocatalytic performance, contributing to sustainable and eco-friendly solutions across various sectors. A simple and reproducible co-precipitation method was employed to synthesize CeO_2, La_2O_3, and CeO_2–La_2O_3 nanoparticles. The physicochemical, optical, and photoluminescent properties of the samples were characterized using FE-SEM, FT-IR, XRD, EDS, Raman spectroscopy, UV-Vis DRS, and photoluminescence spectroscopy. The photocatalytic performance of CeO_2–La_2O_3 nanocomposites was evaluated through the degradation of methylene blue (MB) dye under both UV and solar light.

MATERIALS AND EXPERIMENTAL SECTION

CeO_2, La_2O_3, and CeO_2-La_2O_3NPs were synthesized via chemical precipitation using grade A chemicals from HiMedia Labs, India, including cerium nitrate hexahydrate (99.99%), lanthanum nitrate hexahydrate (99.99%), sodium hydroxide pellets (99.99%), hydrochloric acid (40%), and MB ($C_{16}H_{18}ClN_3S$). Distilled water and ethanol were employed for rinsing, recovery, and solution preparation, with no further purification of the chemicals.

Synthesis of La_2O_3 Nanoparticles

To synthesize the approach 8.6 g of $La_2(NO_3)_3 \cdot 6H_2O$ (0.2 M) dissolve in 100 mL of distilled water. Together, 7.9 g of 2 M NaOH was mixed in 80 mL of distilled water. The NaOH solution was slowly add to the lanthanum precursor while stirring constantly until the pH of the combination became 10. To prevent impurities the resultant mixture was rinsed at least 4 or 5 times with water that was distilled and once with ethanol. Following moisture removal at 80°C, it was crushed into an extremely wellfine residueform and ashing at 500°Cin an incinerator for firing.

Synthesis of CeO_2 Nanoparticles

Similarly, to synthesize cerium oxide, 8.68 g of cerium nitrate hexahydrate ($Ce(NO_3)_3 \cdot 6H_2O$, 0.2 M) was dissolved in 100 mL of distilled water. Separately, 7.9 g of NaOH (2 M) continued liquefiedin 80 mL of distilled water. Sodium hydroxide solution was then gradually added to the cerium solution with stirring, maintaining the pH between 9 and 10. The mixture was agitated under ambient conditions and washed 4–5 times with distilled water and once with ethanol to remove impurities. The resulting mixture was dried at 80°C, ground into well-satisfactoryfine particles, and calcined at 500°C inthe incinerator.

Synthesis of Bimetallic CeO_2-La_2O_3hetero-NC

To create a colloidal suspension, La_2O_3 and CeO_2 powders were mixed in a 1:2 ratio and dissolved in ethanol. In a 200 mL beaker, the mixture was stirred continuously for 2 hours at 60°C using a magnetic stirrer. Lateraeration, the blendpowder was sintered in anincineratorat a similar temp (500°C) for 3 hours, producing a fine light yellow-gray powder.

CHARACTERIZATION TECHNIQUES

The synthesized NPs were studied via a variety of approaches. FT-IR spectroscopy (Nicolet 6700, NIT Srinagar) examined absorption bands (4000-400 cm^{-1}). Materials surface topography and compositions of elements were investigated using FE-SEM (Gemini-500, ZEISS, CRFC NIT Srinagar). The phase transitions and crystallite size were measured using XRD (Rigaku D/max, Cu-Kα, 20-80°). Energy band gaps were measured using UV-visible spectroscopy (Shimadzu UV-3600, 200–800 nm). Raman spectroscopy (RENISHAW InVia, CRFC NIT Srinagar) investigated vibrational modes. The luminescence properties were measured via a fluorescence (Shimadzu RF-5301) spectrophotometry.

Photochatalytic Activity and Measurment

This study evaluated the photocatalytic performance of CeO_2, La_2O_3, and CeO_2–La_2O_3 nanoparticles for the degradation of a 30 ppm methylene blue (MB) dye solution under both UV and sunlight exposure. The UV-driven degradation was conducted in a custom-designed photoreactor with a 500 mL batch capacity. The setup included a central quartz tube housing the UV light source, a water-cooled jacket to maintain thermal stability, and inlet/outlet ports for sample collection. The nanoparticle catalysts were dispersed in the dye solution, and continuous stirring using a magnetic stirrer ensured uniform mixing while minimizing external UV exposure. Samples were withdrawn at regular intervals and analyzed via UV-Vis spectroscopy to monitor MB dye degradation.

In addition, a study was undertaken to evaluate the photocatalytic efficacy of NPs under solar radiation. Experiments were held in June at NIT Srinagar in natural sunshine (12:30-3:00 PM), with air temperatures of 28-31°C, a UV index of ~9, and 59% humidity. A 100 mL MB solution (30 ppm) containing 25 mg/L catalyst was stimulated in theopaque for 30 minearlieroccurrencein visible irradiation. Samples were collected at regular intervals, filtered via Whatman filter paper, and analyzed using a Shimadzu UV-1601 spectrophotometer to determine MB degradation. The degradation percentage was calculated using a standard formula.

$$D\% = [1 - (C_t/C_o)] \times 100 \quad (1)$$

Where C_0denotes the initial reaction and C_t denotes the final reaction under of photochemical reaction that is classified in min.

RESULTS AND DISCUSSIONS

FTIR Analysis

The chemical characteristics of produced samples were identified using FTIR spectroscopy in the 400–4000 cm^{-1} wave number range. Fig. 1 shows that La_2O_3 has a weak absorbance at 3606 cm^{-1} in the infra-redrange, signifying an O-H stretching vibration caused by water molecules adsorbed on the surface[24]. The peak at sharp615 cm^{-1} represents La-O stretchingvibrations, whereas the small, sharp peak at pointed 813 cm^{-1} represents La-O stretching vibrations[24]The peak approximately 1332 $cm^{-1}$is a result of the N-O stretching mode. Whereas the bands at 1062 cm^{-1} correspond to the observed C-O stretching vibration for both La_2O_3 and NC samples. The bands identified at specific wavenumbers in the FTIR spectra, as corroborated by various literature sources, confirm the formation of La_2O_3[25,26]. Fig.1 displays similar results for CeO_2, with two wide-rangingpikesin the FT-IRspectrum. The wide absorption around 3407 cm^{-1} is assigned to the O-H, however, the minor wide signal at 1491 cm^{-1} belongs to the N-O group, suggesting nitrates[27,28].The region at 2360 cm^{-1} peaks represents C-H broadening, while other widemodes at 1329 cm^{-1} and 1062 cm^{-1} are related to C-O vibrational mode in Ramanspectrum.Further,in Ceric oxide, Ce-O bond demonstrat an asymmetric stretching mode that is strongly correlated with a signal at 813 cm^{-1}.

CeO_2nanoparticles can be confirmed by observing for a fingerprint where the O-Ce-O band [28]formed, with a peak at 658 cm^{-1}, is present. Furthermore, the FT-IR spectrum of the successfully synthesized CeO_2-La_2O_3 NC (Figre 1) shows the presence of both the Ceric and lanthanum oxide peaks in the main composite of oxide as well as the validity of the synthesized CeO_2-La_2O_3 NC. Around 3428.30 cm^{-1}, the extensive hump in the CeO_2-La_2O_3 NC spectrum was caused by the mode of stretching due to the O-H presence. The existence of both La_2O_3 and CeO_2 is evidenced by the presence of short points at 615, 813, and 1062 cm^{-1} in FT-IR measurements of the composite and its constituents. The high transmittance at 1432 cm^{-1} is due to the irregular elongation of nitroalkane, which indicates the existence of nitrate in the composite sample.While favors the synthesized NC which holds equally La_2O_3 and cerium oxide functional groups. The slight shifts in the identified peaks are attributed to the doped La and Ce concentrations, indicating significant interaction between the La_2O_3 and CeO_2 NPs in the NC.

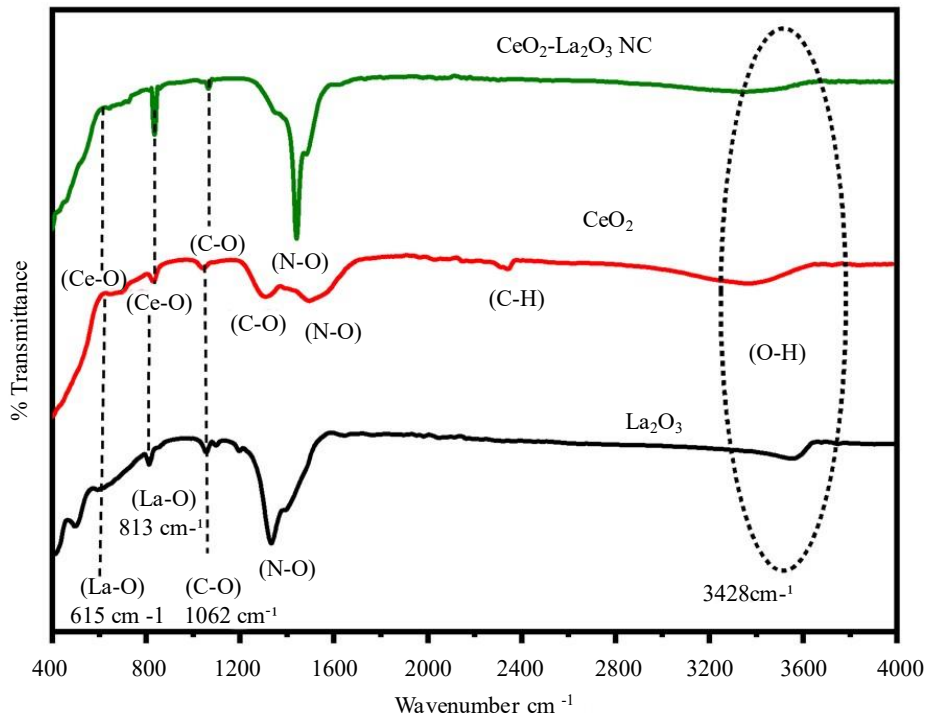

Figure 1. FT-IR spectra of La_2O_3, CeO_2, and CeO_2-La_2O_3 NC.

FE-SEM-EDAX Spectrum and Mapping analysis

The fabricated samples'surfacemorphologiesof CeO_2-La_2O_3NCwere analyzed using FE-SEM with 500 nm resolution. Figure 2(a, b, and c) show FE-SEM images of CeO_2NPs, which have a spherical form and smooth surfaces. Minor aggregation is visible at different magnifications. In contrast, Fig. 2(d) depicts the morphology of La_2O_3NPs, displaying a combination of mismatched flake and spherical morphologies within the same 500 nm range. These morphological changes may have an impact on the photocatalytic performance of individual components as well as the composite.Fig. 2(g, h, and i) show the irregular and partially amorphous morphology of CeO_2-La_2O_3NPs, with agglomerated clusters of different sizes and shapes.

The irregularity is caused by the reduced ionic radii of La^{3+} and Ce^{3+} ions, as well as the lattice strain caused by the mismatch between host and dopant ions[10]. As dopant concentration increases, particle size decreases. The effect of dopant concentration on surface morphology is clear, demonstrating its importance in modifying NP structure.Figure 2 shows also the EDS analysis of CeO_2, La_2O_3, and CeO_2-La_2O_3 s NCs to govern their chemical composition and consistency. The EDS spectra and elemental mappings support the uniform distribution of Ce, La, andO inside the CeO_2-La_2O_3 medium, concerning their weight (Wt. %) and atomic(At. %) percentage of 16.5%, 9.9%, and 73.6%.Furtther, elemental mapping at a 50 µm scale confirms the uniform distribution of these elements, no other element or impurities present in composite samples. The identicalintegration of lanthanum and ceric components throughout the composite promotes the establishment of a One-phase appearance. These findings support the occurrence of heterojunctions regardingCe and La, emphasizing their importance in making an efficient hybrid NC.

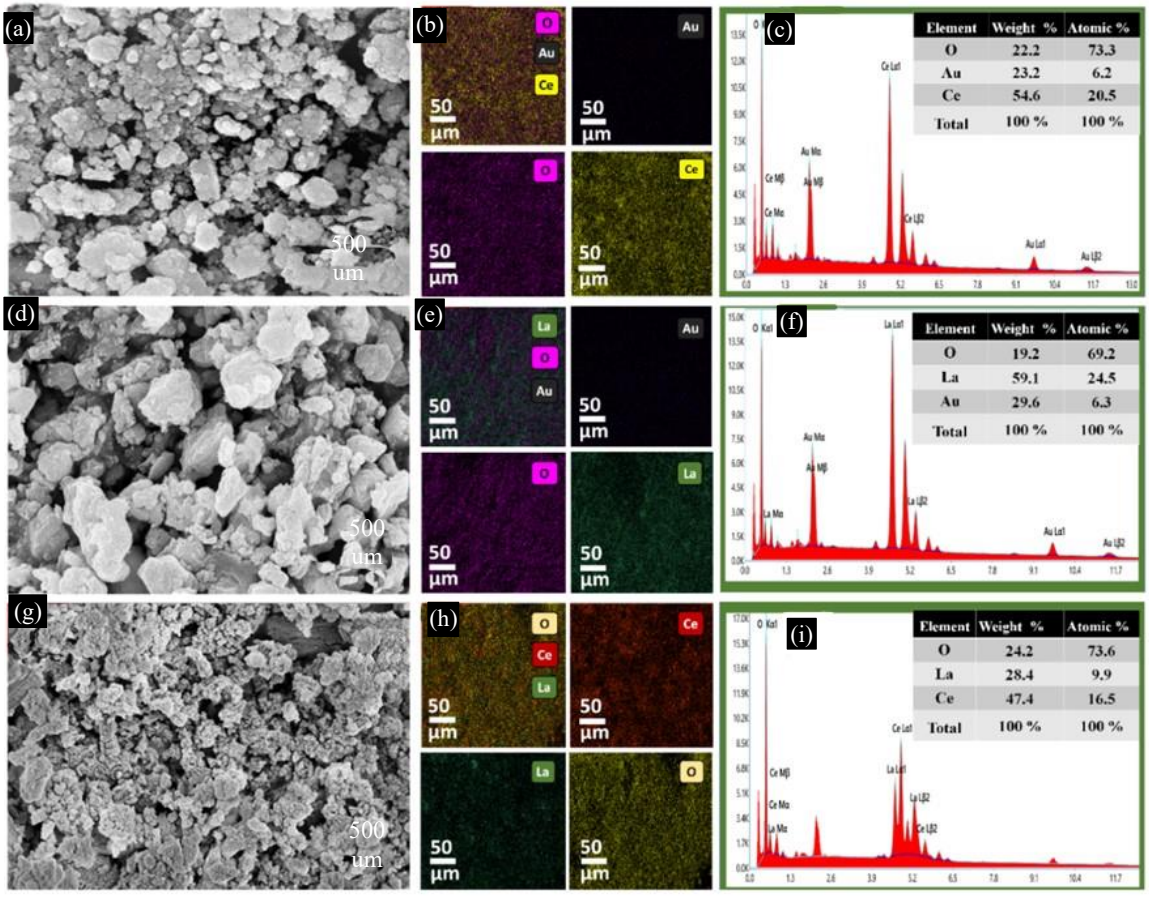

Figure 2. FE-SEM, EDX dot mapping, and elemental composition of NPs, (a-c) CeO_2, (d-f) La_2O_3 (g-i) CeO_2- La_2O_3 NC.

X-Ray Diffractionanalysis

X-ray diffraction (XRD) validated the making and crystallographic analysis of the synthesized CeO_2, La_2O_3, and the bimetallic CeO_2-La_2O_3 hetero-NC, as shown in Figure 3. The XRD patterns show different plasmon peaks in all three materials.CeO_2NPs exhibited diffraction peaks at 28.55°, 33.07°, 47.90°, 56.32°, 69.40°, 76.73°, 71.37°, 79.07°, and 88.45°, correspondent to the (111), (200), (220), (311), (222), (400), (331), (420), and (422) planes, respectively. These results are consistent with the cubic fluorite structure of CeO_2, as confirmed by JCPDS card no. 43-1002, showing efficient fabrication of CeO_2NPs[29].The XRD pattern of pure La_2O_3NPs showed peaks at 25.32°, 27.72°, 28.93°, 37.90°, 44.63°, 49.72°, 52.01°, 53.36°, 54.07°, 57.26°, 59.95°, 63.60°, 72.64°, 75.38°, and 79.26°. These peaks correspond to the (100), (002), (101), (102), (110), (103), (200), (112), (201), (004), (202), (104), (211), (114), and (105) crystallographic planes, which conform to the hexagonal phase of La_2O_3as identified by JCPDS card no. 83-1348.Previous research, including those by Kabir et al.[30], supports the successful making and phase purity of CeO_2 and La_2O_3, as well as the creation of the CeO_2-La_2O_3 hetero-NC.The XRD patterns show a reduction in the intensity and clarity of CeO_2 peaks in the CeO_2-La_2O_3 NC, suggesting a decrease in CeO_2 crystallinity after La_2O_3integration.The CeO_2-La_2O_3 NC's diffraction peaks are similar to those of pure CeO_2 and La_2O_3, with no extra peaks, indicating that the composite is made entirely of these two oxides. The XRD data imply the fabricated sample of a solid solution assisted by a simple precipitation synthesis procedure carried out at high temperatures.Fig. 3(b) shows small shifts in La_2O_3 peaks from lower to higher angles, including 29.92° to 30.32°. These peak shifts and broadenings confirm the inclusion of La^{3+} ions into the CeO_2 lattice.

This lattice distortion favors the effectiveaddition of La_2O_3 into the CeO_2 matrix, as previously seen in similar investigations[31].Figure 3(b) shows the elimination of minor lanthanum oxide peaks at 29.12° in the CeO_2-La_2O_3 composite. This can be attributed to the creation of a solid solution, crystal lattice deformation, increased homogeneity, and probable phase transitions during synthesis. These occurrences alter diffraction patterns, confirming the successful integration of La_2O_3 and CeO_2 into the composite material.The XRD patterns of CeO_2-La_2O_3 NCs demonstrate a decrease in the intensity and sharpness of CeO_2peaks, representing reduced crystallinity of CeO_2 with La_2O_3 insertion. The structural changes can be ascribed to lattice alteration caused by the substitutional or interstitial insertion of La^{3+} ions into the CeO_2 lattice. This alters peak intensities and positions.

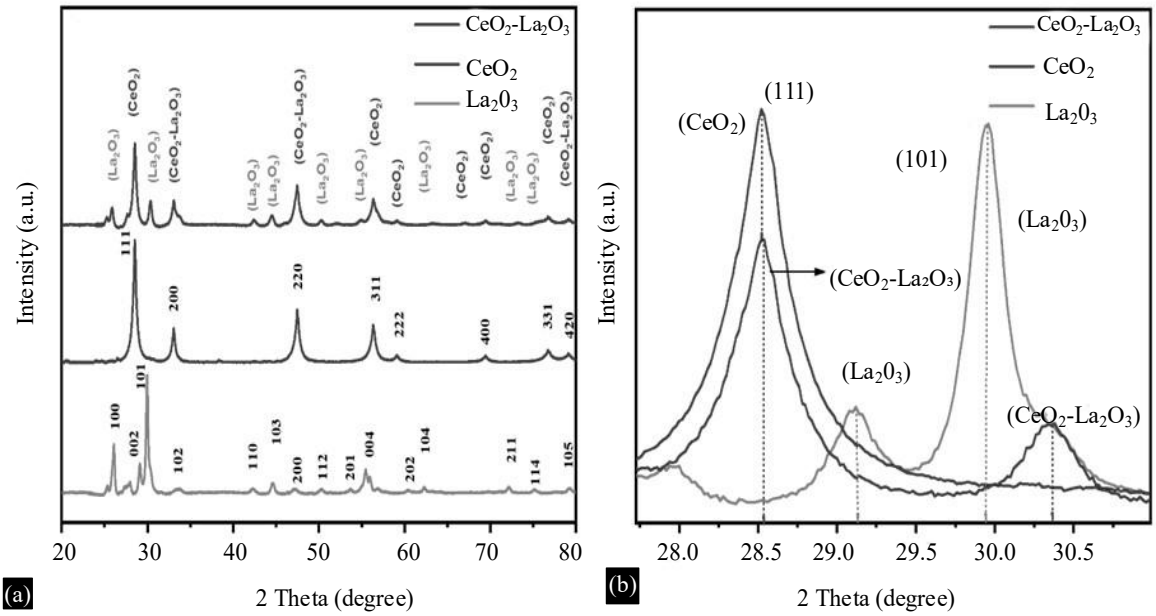

Figure 3. (a) XRD patterns of La_2O_3, CeO_2, and CeO_2–La_2O_3 NCs; (b) Peak shift and broadening indicating structural variation in the composite.

Table 1. Estimated average crystallite size for all prepared NPs with FWHM values at varied theta angles.

Materials	2 Theta	FWHM (deg)	Crystallite size (nm)
La_2O_3	29.95	0.346	22.18
CeO_2	28.51	0.530	12.79
CeO_2-La_2O_3	28.53	0.602	14.50

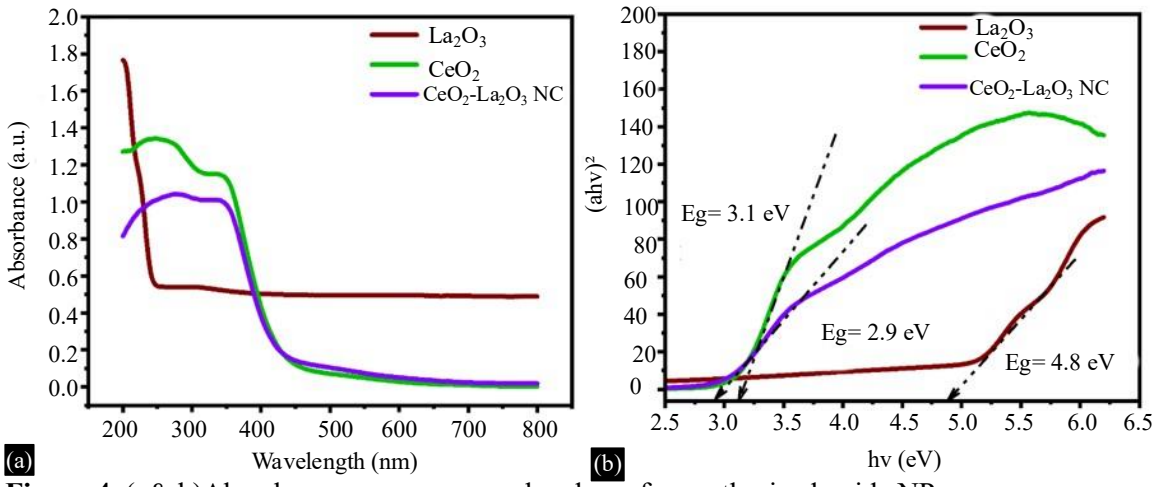

Figure 4. (a& b)Absorbance verses energy band gap for synthesized oxide NPs.

The crystallite size of the synthesized NPs was calculated using Scherrer's equation:

$$D = \frac{k\lambda}{\beta Cos\theta} \quad (2)$$

Where D is the average crystallite size, k is the shape factor (typically 0.9), λ designateX-ray wavelength(1.5406 Å for Cu-Kα), $\beta$is full and half maxima *(FWHM)* of the XRDapex in radians, besides θ is the diffraction angles. This study providesadditional insights into the nanoscale proportions of the synthesized materials and corroborates the structural changes induced by La_2O_3 incorporation.Table 1 presents the average sizes of crystallites for the materials in their as-synthesized state.

UV-vis Spectroscopy Analysis

The optical properties of synthesized La_2O_3, CeO_2, and CeO_2-La_2O_3 nanostructured materials were analyzed withUV-vis spectroscopy. Hence, the energy band gap of the fabricated samples was analyzed by performing an absorption measurement at room temperature. Optical absorbance measurements show that La_2O_3, CeO_2, and CeO_2-La_2O_3 NCs all absorb ultraviolet light at wavelengths shorter than 400 nm. Absorption spectra of La_2O_3 nanoparticles as a function of wavelength are shown in Figure 4(a).

By using the Tauc plot correlation in Eq. (3)[32], we were able to determine the optical energy band gap (E_g) for synthesized La_2O_3 NPs by analyzing the transition between the valance and conduction band. Tauc relation expression of $(ahv)^2$ versus hv was used to determine the estimated energy bandgap (E_g) of La_2O_3 Oxide, which was found to be 4.8 eV (Figure 4(b).

$$\alpha h\nu = A(h\nu - Eg)^n \quad (3)$$

In this relation "$h\nu$" represents the energy of a photon, "α" represents the coefficient of absorption, while, 'A' represents the nanoparticles proportionality constant, and 'n' is the transition potential, where n = 2 for direct transitions and n = 1/2 for indirect ones.Fig. 4(a–b) shows the absorbance vs. wavelength plot and the estimated band gap of CeO_2 (~3.1 eV) calculated using the Tauc relation. Similarly,

absorbance versus wavelength measurements for CeO_2-La_2O_3 NCs yielded an estimated energy bandgap *(E_g)* of 2.9 eV, as shown in Fig. 4(a&b), which is less than that of pure La_2O_3 and CeO_2 NPs.As particle size decreases in nanostructures, the band gap values of synthesized CeO_2-La_2O_3 NCs reduce. Fig 4 (b) depicts this trend. Quantum confinement effects are accountable for the decrease in the band gap. Quantum confinement restricts the movement of free electrons and holes when a material is enclosed in a space smaller than its characteristic wavelength. When CeO_2-La_2O_3 NC particles attain a nanoscale size, confinement increases, which influences band gap values[33]. The decrease in band gap values impacts the optical and electrical properties of CeO_2-La_2O_3 NCs.

Raman Analysis

A Raman study was performed from the created samples within the groupof 200-1600 cm^{-1}. Fig. 5 shows Raman spectra (La_2O_3, CeO_2, and CeO_2-La_2O_3 NC) obtained with a Renishaw inVia spectrometer.

Spectrum analysis is commonly used to identify samples' low-frequency, low-vibrational, and rotational modes. In the current investigation, the excitations for La_2O_3 NPs were observed in four distinct band positions specifically at 283 cm^{-1}, 341cm^{-1}, 449 cm^{-1}, and 1086 cm^{-1} respectively (Fig. 5). It has been determined that Raman bands correspond to these bands. In the prior research, a variety of different theoretical and experimental Raman shifts were reported. The peak at 341 cm^{-1} corresponds to the La-O vibration, while the band at 449 cm^{-1} corresponds to the Egv1 mode documented by the other authors [34],[35].Additional spectrum bands (341 cm^{-1}, 283 cm^{-1}, and 1086 cm^{-1}) detected in this study have been stated in a similar location by other investigators [35]. Similarly, the Raman shift at 1086 cm^{-1} supports the surface carbonate and hydroxide compounds [35], [23]. Further CeO_2 only displays the T2g Raman mode due to its fluorite-type cubic structure. The symmetrical vibration of Ce-O-Ce is to blame for this effect [35]. Raman spectra were observed in this study from a single Raman shift at 465 cm-1 with an extremely broad intensity distribution to Fig. 5. Similarly, the band spectrum of the CeO_2-La_2O_3 NCs is depicted in Figure 5. where the La_2O_3 and CeO_2 peak intensity matched its position in the CeO_2-La_2O_3 NCs. This has already been discussed in the above explanation. This investigation's findings indicate that there were no additional symmetric adjustments or modifications that could potentially explain the Raman shift.

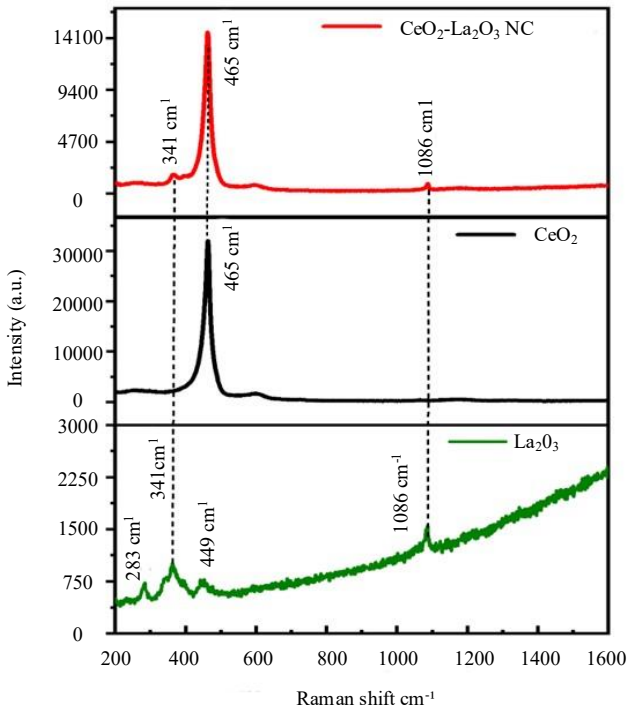

Figure 5. Raman spectrum for the synthesis of a CeO_2, La_2O_3, and a CeO_2-La_2O_3 NC.

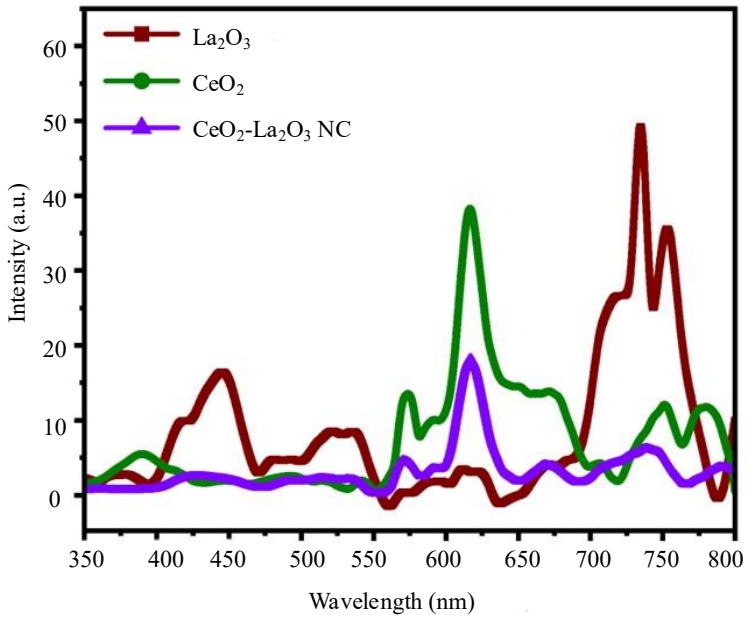

Figure 6. Photoluminescence spectra for CeO_2, La_2O_3, and CeO_2-La_2O_3 NC.

Photoluminescence Study

PL analysis was also used to investigate the luminous characteristics of produced oxide NPs. PL measurement, which relies on photoluminescence data, is the most effective method for investigating semiconductor materials' optical and electrical structure, such as band gap creation and photoinduced charge carrier recombination [34]. As shown in Fig. 6, the study observed the luminescence characteristics of pure CeO_2, La_2O_3, and CeO_2-La_2O_3, NPs for photo-generated electron excitations in the 350-800 nm range at room temperature. The spectral range of Fig. 6 covers the photoluminescence analysis of high-purity CeO_2, La_2O_3, and CeO_2-La_2O_3NPs. Pure La_2O_3 (325, 440, 529, 742, and 752), CeO_2 (380, 560, 620, and 750), and CeO_2-La_2O_3 nanoparticles (418, 560,620, and 740) exhibited significant PL intensity signals over a broad spectrum of wavelengths. La_2O_3 intensity was highest in the 742 nm wavelength range. Similarly, CeO_2 exhibited the highest PL intensity at 620 nm. CeO_2 reaction with La_2O_3 substantially reduced the luminescence intensity of the observed emissions and caused their positions to shift slightly.

Introducing La_2O_3 into the CeO_2 lattice may induce an effect of disorder, which may explain the PL peak intensity placements associated with heterojunction between CeO_2-La_2O_3 nanostructures[35].This finding raises the possibility that doping between La_2O_3 NPs and CeO_2 can minimize surface defects for electron-hole pair recombination rate at an interface [34].The enhanced efficacy of the NC as a photocatalyst was established by its luminescence intensity being less than that of pure metal NPs. This was a result of the effective photoexcited electron-hole pair recombination rate. Based on the preceding findings, the analysis of the CeO_2-La_2O_3 composite at the minimized peak position in the PL spectra revealed a decrease in charge relocation mobility and defect presence in the composite samples with La in the ceric structure. These results indicate a reduction in the rate of electron-hole pair recombination, leading to improved photocatalytic performance [36].

Photocatalytic Performance and Mechanism Study

Catalytic activity and photocatalytic performance of as-synthesised CeO_2, La_2O_3, and CeO_2-La_2O_3 NCs in the presence of UV/visible light are investigated throughout the study using MB dye as a pollutant sample. MB dye was decomposed by dissolving 25 mg photocatalyst in 30 ml of MB (30 ppm)dye solution. The removalof dye over doped and undoped samples was studied using a colorimetric technique. For this experiment, a dye solution with a pH of 12 was used as an alkaline medium across all catalysts. For 30 min before illumination, the MB dye solution was stored in a dark

place to allow the catalyst and dye to reach adsorption/desorption equilibrium.At specified time intervals, 5 ml samples of the solutions were taken and centrifuged at 3000 RPM for 5 min. To assess the concentration of the absorbed soluion, using the Whatman [40] Filter paper, the centrifuged solution was filtered. The UV-Vis spectrophotometer (Shimadzu UV-1601) was employed to determine the light absorption characteristics of MB, revealing that it exhibits the maximum absorbance at a 664 nm range. Each catalyst exhibited a continuous and efficient operational cycle when tested individually at numerous time period.

Figure 7 depicts the decomposition of MB dye using a nanocatalyst composed of CeO_2, La_2O_3, and a CeO_2-La_2O_3 composite, subjected to varying response times ranging from 0 to 100 minutes in UV light conditions. When the rate of reaction is enhanced, the MB dye exhibits a decrease in light absorption, indicating a rapid of degradation. The utilization of CeO_2, La_2O_3, and CeO_2-La_2O_3NPs as catalysts is presented in Figure 7 considering the UVregion. Figure 7(a) depicts the reaction kinetics for the degradation of MB dye employing various catalysts at different time intervals, under both UV irradiation conditions. All of the samples begin with the same concentrations of contaminants, pH, and catalyst dosage, but the reaction times differ. The NC catalyst of CeO_2-La_2O_3degrades quickly in comparison to nanoparticles of La_2O_3 and CeO_2. The experimental outcomes of the catalytic deprivation of MB dye using CeO_2-La_2O_3 NC catalysts in the research environment are depicted in Fig. 7(d). In addition, the efficiency and effectiveness of the catalyst for all prepared samples were also evaluated under visible light conditions, the given conditions have already been mentioned in the photocatalytic investigation section.

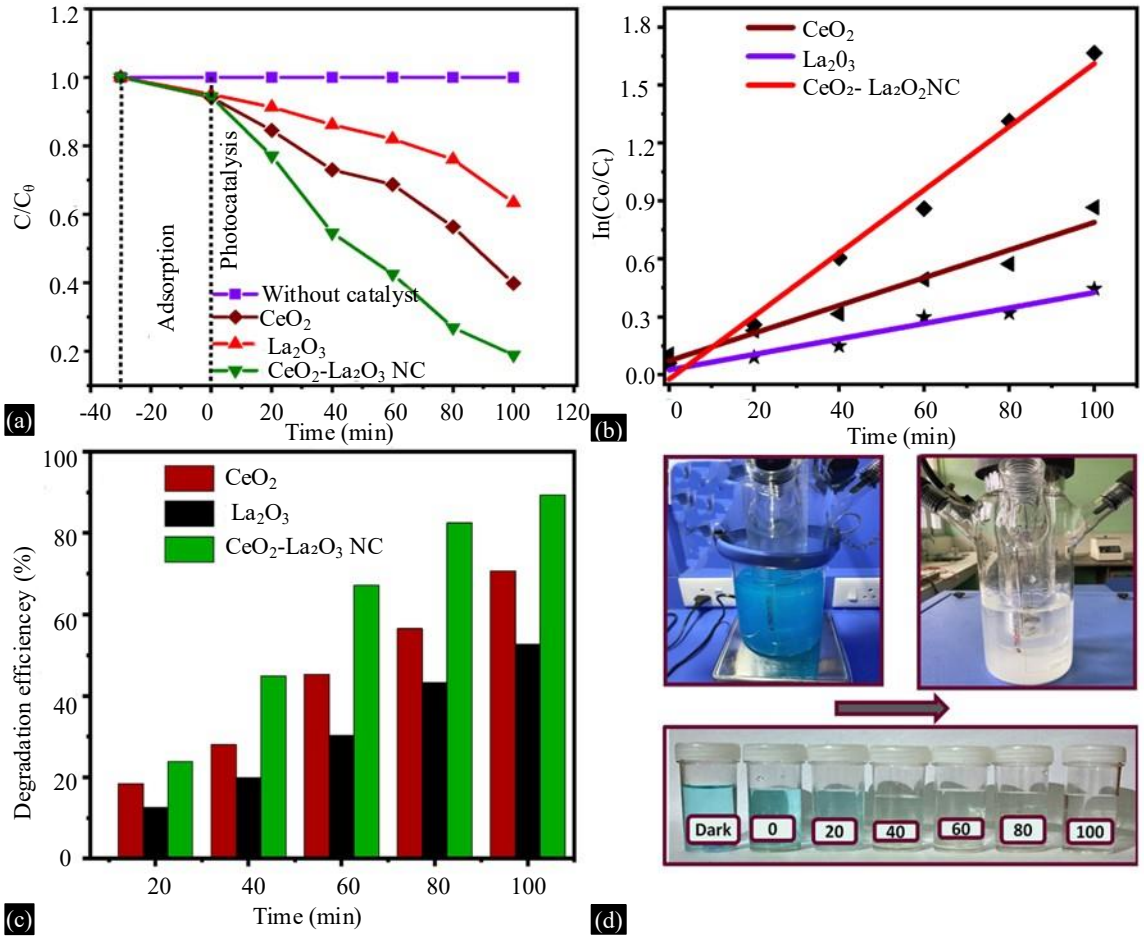

Figure 7. (a) Degradation curves of MB using individual oxide NPs; (b) Kinetic plots of MB degradation with different NPs; (c) Degradation efficiency of MB in the presence of catalysts; (d) Photocatalytic activity of CeO_2–La_2O_3 NCs under UV light at various time intervals.

The experiments were conducted under UV irradiation for a duration of 0-100 min and under solar irradiation for 0-180 min. Similarly, a research endeavor was also conducted to examine the degradation of MB dye under solar irradiation, employing NPs as catalysts. The objective was to assess the efficacy of these catalysts under visible light conditions, as well as to conduct a comprehensive analysis under UV conditions, as depicted in Fig. 8 In the identical time-based period, the results of conventional oxide and altered CeO_2-La_2O_3 blends are depicted in Fig. 8(d). The aforementioned results are observed during the time frame of 12 pm to 3 pm in June, at the Nit Srinagar campus, utilizing solar energy, throughout 0 to 180 min. The photocatalytic degradation rate constants (k, min^{-1}) for all samples under UV/visible irradiation are shown in Table 2. Where Fig. 7(a) and 8(a), show the time-dependent ln (C_0/C_t) representation of the photodegradation reaction rate constants (k, min^{-1}). Pseudo-first-order kinetics in Eq. (4) is fitted using a curve-fitting method for both UV and visible regions[35][31].

$$-ln\left(\frac{C_t}{C_o}\right) = -kt \quad (4)$$

The starting and endingdye aresignified by the letters $C_0$and C_t, correspondingly. 't' represents the stage ittakes for the energy source (Uv/visible) to irradiate the dye, and 'k' denotes the Pseudo-first-order kinetics and its rate costant value, which were expressed in min^{-1}.The Pseudo-first-order kinetics follow for all the synthesized La_2O_3, CeO_2, and CeO_2-La_2O_3 NC samples under both UV and solar irradiation. Under UV irradiation, the kinetics constant proportion (k) min^{-1} for undoped La_2O_3 NPs are 0.00374, for CeO_2 NPs they are 0.00738, and for CeO_2-La_2O_3NC they are 0.01637 min^{-1} based on the slope and intercepts.In addition, the calculated estimated rate constants (k, min^{-1}) for solar irradiation are 0.00400 for undoped La_2O_3 NPs, 0.00693 for CeO_2 NPs, and 0.01002 min^{-1} for CeO_2-La_2O_3NC. The rate constants (k, min^{-1}) for pure La_2O_3 and CeO_2NPs exhibit lower values in comparison to CeO_2-La_2O_3NC when subjected to both solar and UV irradiation, as indicated by the slope and intercept for Figures. 7(b) and 8(b).

This implies that NC has highly effective and beneficial catalytic properties under both solar and UV light conditions. Table 2 also shows the different dosages, rate constants (k), correlation coefficients (R^2), and concentrations for MB deterioration at the formed photocatalyst appropriate for both UV and solar irradiation. Figure.7(c) and Figure. 8(c) illustrate the photodegradation percentage (D%) achieved by employing CeO_2, La_2O_3, and CeO_2-La_2O_3 nanoparticles at different time intervals during the reaction process, both under Uv and solar irradiation conditions.The CeO_2-La_2O_3 composite exhibited a higher degradation efficiency of 93% after 100 min under UV light and 96.66 % after 180 min in the presence of natural solar light, in contrast to the deteriorationeffectiveness of pure oxide NPs. Further, Table 2 depicts a relative study of MB dye when subjected to ultraviolet and solar irradiation.The Table includes the respective kinetic parameters obtained under various optimized conditions for the catalyst used in the study.

The photocatalytic performance of the as-prepared bimetallic CeO_2-La_2O_3 hetero-NC was compared to the previously reported photocatalytic activity of several different catalysts, which can be seen in Table 3. Table 3 also presents a comparative analysis of the photocatalytic performance of CeO_2, La_2O_3, and their bimetallic heterostructured composites, along with results from previously reported studies by various researchers in this field. The table highlights various CeO_2-based photocatalysts, often doped or coupled with other materials, and their efficiency in degrading different pollutants under diverse light sources. Notably, the present study demonstrates that the bimetallic CeO_2-La_2O_3 heterocomposites exhibit superior photocatalytic activity, especially for the degradation of MB dye compared to previously reported systems. This makes it more appealing for dye degradation, specifically MB dye. The enhanced photocatalytic activity at the CeO_2-La_2O_3 ratio can be attributed to the optimized interfacial contact between p-type La_2O_3 and n-type CeO_2, which facilitates the formation of an effective p–n heterojunction. This promotes efficient charge separation and transport while minimizing recombination.

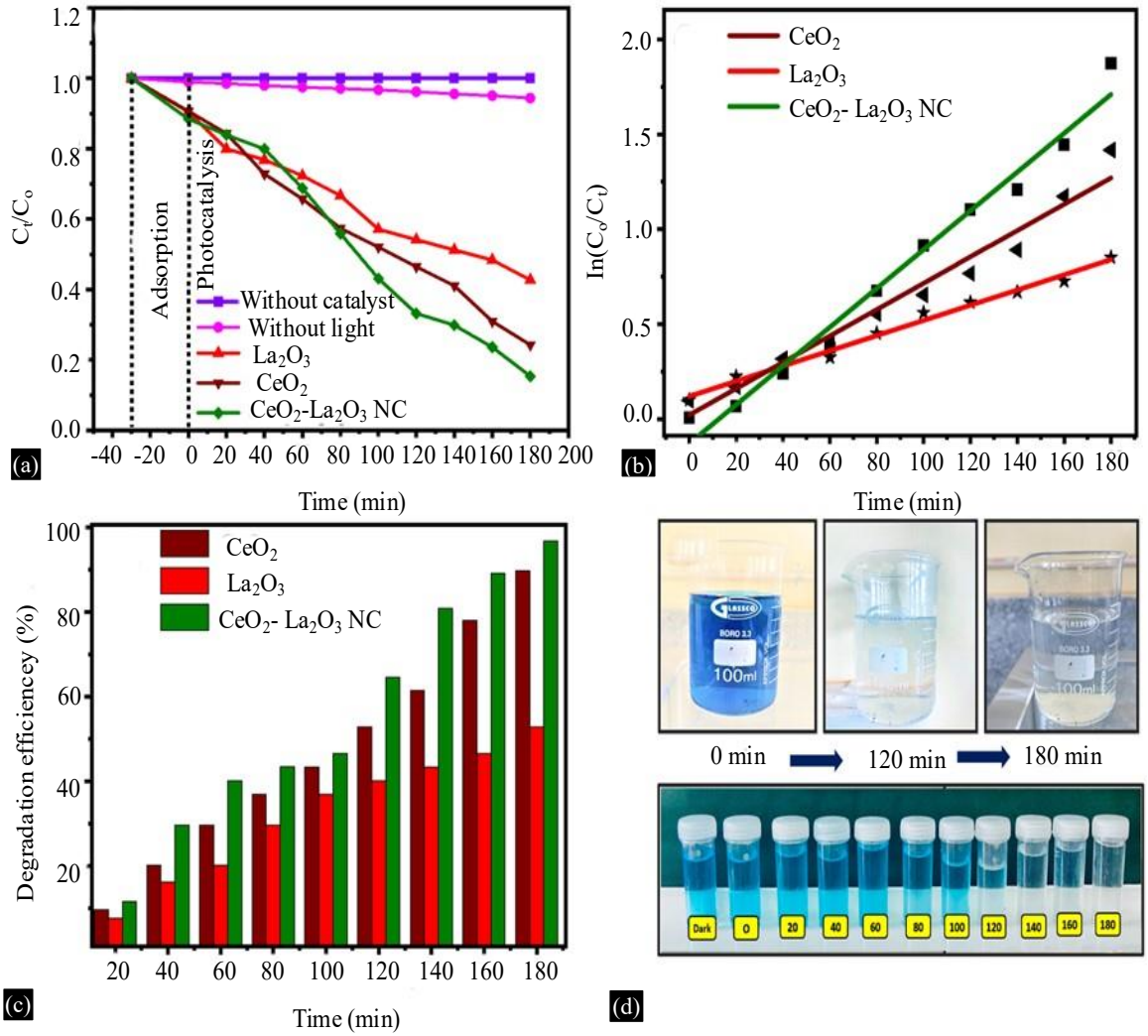

Figure 8. (a) Degradation curves of MB using individual oxide NPs; (b) Kinetic plots for MB degradation with different NPs; (c) Degradation efficiency (%) of MB in the presence of catalysts; (d) Photocatalytic performance of CeO_2–La_2O_3 NCs under solar light at various time intervals.

Table 2. Degradation activity and rate constants of oxide samples under UV and solar light.

Light source	Prepared catalyst	Pollutant Conc. *(ppm)*	Doses conc.*(mg)*	Time duration*(min)*	CatalystEfficiency*(%)*	Rate constant*(min^{-1})*	Correlation coefficients*(R^2)*
Uv light							
	CeO_2	30	25	100	78.46	0.007389	0.9616
	La_2O_3	30	25	100	58.67	0.003743	0.9534
	CeO_2-La_2O_3	30	25	100	93.34	0.016348	0.9849
Solar light							
	CeO_2	30	25	180	89.61	0.006938	0.9681
	La_2O_3	30	25	180	53.82	0.004005	0.9884
	CeO_2-La_2O_3	30	25	180	96.66	0.010022	0.9770

Table 3. Comparison of photocatalytic degradation of organic pollutants by various binary metal oxide photocatalyst.

Catalyst	Organic pollutant	Light source	Catalyst doges (g/L , mg/L)	degradation (%)	Irradiation time (min)	References
CeO_2/ZnO	Methylene Blue	UV	175 mg/L	67.4	90	[37]
CeO_2/La_2O_3	Rhodamine-B	UV	30 mg/L	70	150	[35]
La-doped SnO_2	Methylene Blue	UV	25 mg/L	94	75	[38]
La-doped ZnO	Methylene Blue	UV	0.1 g/L	80	60	[39]
La_2O_3/TiO_2	Rhodamine-B	Visible	10^{-5} M	56	200	[40]
La-doped ZnO	Methylene Blue	Solar light	10 mg/L	NA	100	[41]
La_2O_3/SnO_2	Methylene Blue	UV	50 mg/L	92	70	[23]
TiO_2/La_2O_3	Methylene Blue	UVVisible	0.1 g/L0.1 g/L	9527	120120	[42]
La-doped ZnO	Rhodamine- B	UV	-NA	NA	200	[43]
CeO_2/La_2O_3	Methylene Blue	Solar light	20 mg/L	96	180	This study
		UV	20 mg/L	93	100	

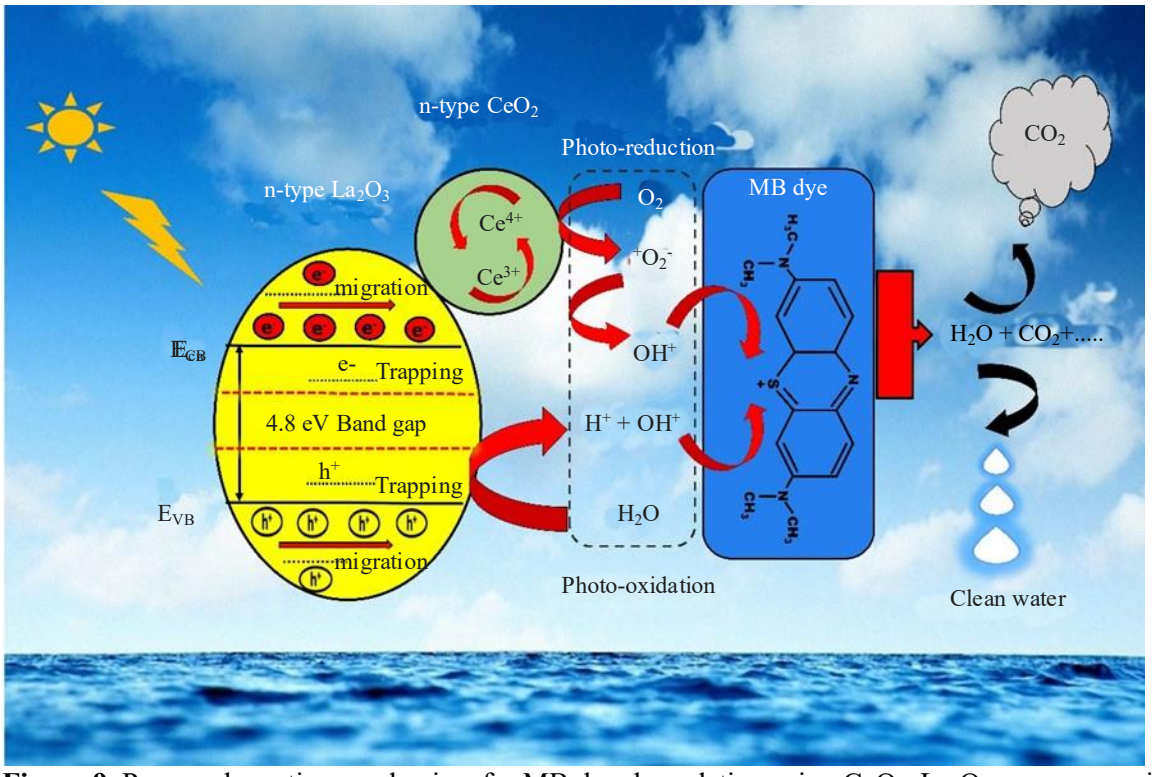

Figure 9. Proposed reaction mechanism for MB dye degradation using CeO_2–La_2O_3 nanocomposites.

Further, Figure 9 depicts the results derived for the photocatalytic degradation mechanism for the proposed UV/visible light mechanism of CeO_2-La_2O_3 photocatalysts. Generally, in the oxidation phase of an industrial effluent system, photocatalytic degradation in the presence of a catalyst is used to convert dyes into water, carbon dioxide, and other by-products. A catalyst having a bandgap active with visible or ultraviolet light is used to speed up the reaction without being depleted in the process. The effectiveness and efficiency of photocatalysts depend on several factors such as particle sizes, UV light

exposure, electron-hole pair recombination rate, solution pH, dye concentration, reaction temperature, and dye saturation [44]. Photocatalytic degradation processes of dye pollutants under an irradiated energy source in the presence of photocatalysts primarily involve reactive oxygen species (ROS). The most commonly observed ROS aresuperoxide anion radicals ($\bullet O_2^-$), hydroxyl radicals (•OH), andholes (h^+), which play a significant role in the degradation of pollutants[45].Fig.9 is a schematic depiction ofMB dye decomposition with heterojunction between CeO_2-La_2O_3-based NC used as a photocatalyst.Excitons are produced when a doped CeO_2-La_2O_3NPabsorbs a photon with a higher or equivalent energy bandgap [35].The e^- and h^+ may be transferred to the NPs' faces if the electric charge of a shield remains unaltered throughout the activity. Because of the abundance of oxygen and water molecules in the environment, highly charged e^-/h^+ couples interact with unstable intermediates and engage in aquatic organic targets through oxidation/reduction steps.It is necessary to comprehend the oxidation potential and energy band gap of e^-/h^+ pairs. This aids in identifying the pathway of MB dye breakdown. Additionally, it increases the integrated semiconductors' photocatalytic performance[45]. Where this investigation equation 5 & 6 was used to analysethe electrons and holes position in respective oxide samples.

The estimated relative positions of the conduction (E_{CB}) and valance (E_{VB}) band edgefor fabricated oxide NPs shown in Table 3 from Eq. 5 & 6.

$$E_{CB} = \chi - E_e - 0.5E_g \quad (5)$$

$$E_{EV} = E_{CB} + E_g \quad (6)$$

Where E_{CB} is the band edgeposition from conduction and E_{VB} is the band edgeposition of valence band. While 'E_e' normal hydrogen electrode (NHE) electron energy label (approximately 4.5 eV) [46,47]. Wherever 'E_g' is the valued energy gap between La_2O_3 and CeO_2 semiconductor materials. The electronegativity (χ) of CeO_2 is 5.56 eV, while that of La_2O_3 is 5.50 eV[48],[49]. Using these two Eqs, (5) and (6), we were able to determine the band locations of the semiconductor materials La_2O_3 and CeO_2; the results are displayed in Table 4 and Fig.10.CeO_2's CB and VB band edges were considered to be -0.59 and 2.51 eV, individually, using the aforementioned equations. The VB and CB edge potentials for La_2O_3 were measured to be 3.66 and -1.14 eV. It has been hypothesized that photocatalyst irradiation activates the creation of photogenerated electrons and holes in CeO_2-La_2O_3NCs.Excited electron (e^-) travel from lanthanum CB to the CB band of CeO_2 due to the difference in their band edge potentials (-1.14 eV ~ -0.59 eV). By reacting with the adsorbed MB dye molecules, the • O_2^- (superoxide radicals) and OH• (hydroxyl radicals) are formed, which in turn react with the absorbed O_2 molecules to convert the MB dye molecules into less toxic CO_2, water, and another by-product.

Since CeO_2's VB edge (+2.51 eV) for oxidation reactions is less positive than La_2O_3's (+3.66 eV), the photogenerated holes in CeO_2's VB simultaneously migrate to La_2O_3's VB. Reacting holes and OH produce active oxidizing species, which are used in the VB of La_2O_3 by reacting to the MB dye molecules.The e^- interacts with CeO_2, converting Ce^{4+} to Ce^{3+} due to its unsteady oxidation state. Fig. 9 shows the migration of an O_2 to the photocatalysts on the surface.These highly energetic electrons can take different pathways when they are exposed to ultraviolet or visible light. The e^- of the La_2O_3 VB traveled to the Ce *4f* state before being converted from Ce^{4+} to Ce^{3+}, as seen in Figure 9. The charge difference allows Ce^{3+} to migrate its e^- to the outside, where it responds with O_2 to generate reactive superoxide anion free radicals.Following that, hydroxyl radicals were produced as a result of the interaction between $O_2$and positively charged ions in the aqueous solutions. Similarly, the h^+ in the VB combines with the H_2O, hydroxyl radicals develop at the bottom of the valance band.

Table 4. La_2O_3 and CeO_2 semiconductor calculated band edge.

Catalyst	E_g(eV)	E_{CB}(eV)	E_{VB}(eV)	Electronegativity(χ)(eV)	References
La_2O_3	4.8	-1.14	3.66	5.28	[50]
CeO_2	3.1	-0.59	2.51	5.56	[51]

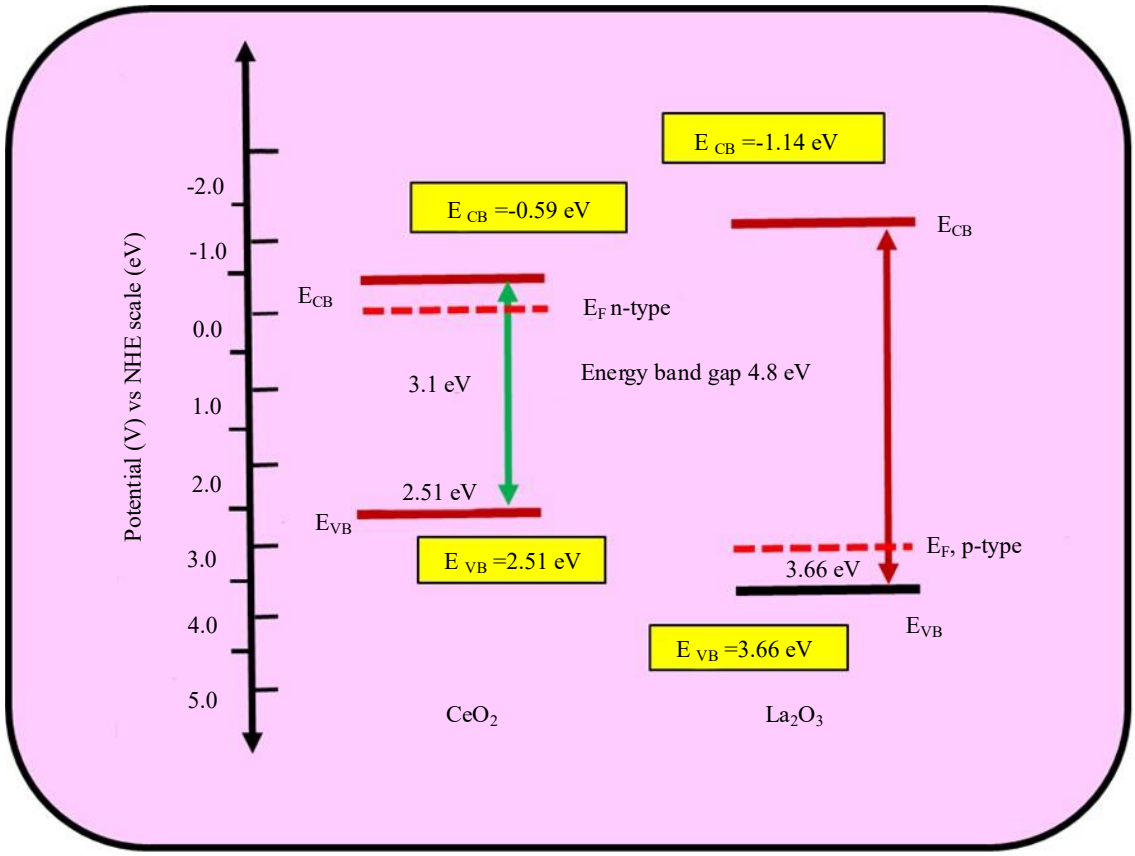

Figure 10. Band edge positions for La_2O_3 and CeO_2 nanoparticles.

These hydroxyl radicals convert the MB dye to CO_2 and H_2O, as demonstrated in Figure 9, which displays the photocatalytic degradation of a CeO_2-La_2O_3oxide-based NC. As a result, the CeO_2-La_2O_3NC demonstrated activee$^-$/h$^+$pairs, demonstrating its exceptional stability and photocatalyst properties for the decay of the MB in the presence of visible/UV irradiation. In addition, band alignment outcomes also confirm the advantageous establishment of a p-n heterojunction composed of CeO_2 and La_2O_3 NCs. This investigation demonstrates a frequent little effort from authors related to this field. The assessment of the catalytic effect of NPs that were successfully synthesized in the decomposition of MB dye was conducted by subjecting them to UV and solar light under different concentrations of catalyst and durations of irradiation, followed by a comparative analysis. Additional study is required to understand how peroxide, pH levels, impurities, and the use of different amounts of catalysts affect the process. These studies may help us learn more about how chemicals break down and remove dyes when they are assisted by outside factors. This research could help us understand how photocatalysis can be used in real-world applications.

Recyclability Study

Photocatalytic performance and catalytic reusability are important parameters in the photocatalystdevelopment. To assess reusability, the most effective catalyst was recycled four times under the same photocatalytic conditions for both UV and solar irradiation. Following photodegradation, the photocatalyst NPs were removed from the solution by centrifugation at 3,000 RPM for 10 minutes. The recovered nanoparticles were extensively washed with deionized water and ethanol and dried for 2 hours at 90°C. Following the completion of the previous cycle, the photocatalyst was prepped for usage in the next photodegradation cycle by adding a fresh MB dye solution.After four usage and revival cycles, the bimetallic CeO_2-La_2O_3 hetero-nanocomposite maintained removal efficiencies of 80.47% under UV light and 84.57% under solar light. Figure 11 depicts the photocatalyst's reusability across various periods under UV and solar irradiation conditions.

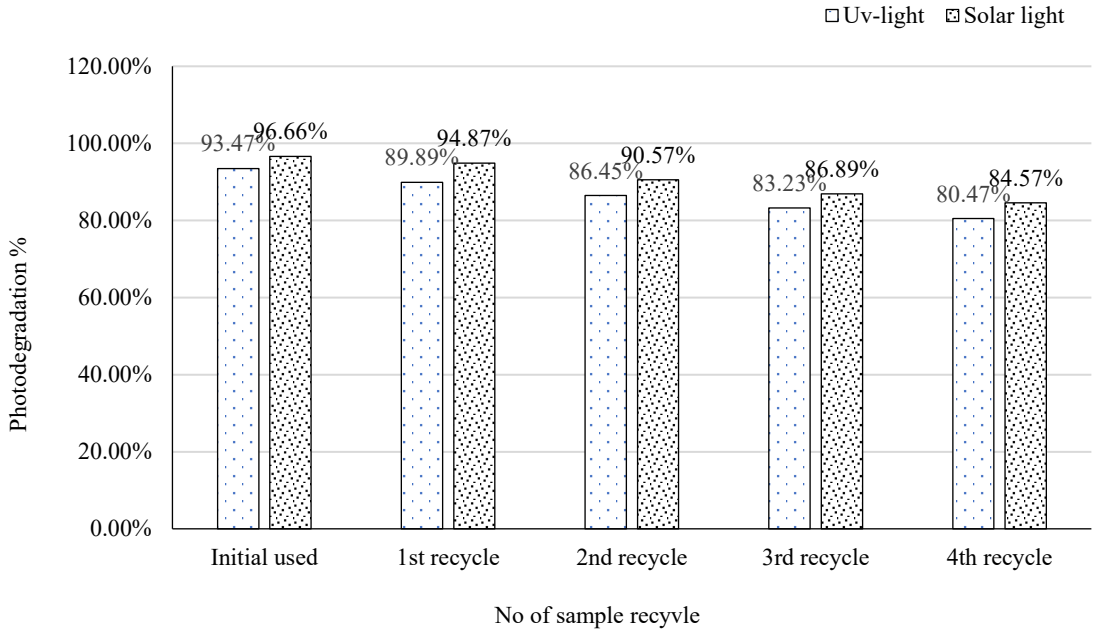

Figure 11. MB dye degradation after four consecutive cycles for CeO_2-La_2O_3 photocatalysts.

The CeO_2-La_2O_3 hetero-nanocomposite exhibited useful renewal and recovery potential, making it an appealing option for reducing effluent pollutants such as MB dye.

CONCLUSION

In summary, CeO_2, La_2O_3, and bimetallic CeO_2–La_2O_3 hetero-nanocomposites (NCs) were successfully synthesized via a simple and cost-effective coprecipitation method. Comprehensive characterization confirmed their structural, morphological, and optical properties. XRD analysis verified the formation of pure crystalline phases with an average crystallite size of ~14 nm. SEM images revealed spherical to semi-spherical nanoparticles with flake-like structures, while elemental mapping confirmed uniform distribution of Ce, La, and O. FT-IR identified key functional groups, and UV-DRS analysis indicated strong light absorption with estimated band gap energies. PL spectroscopy revealed reduced charge carrier recombination in the bimetallic NC, indicating enhanced photocatalytic potential.Photocatalytic activity, evaluated using MB dye under UV and solar light, followed pseudo-first-order kinetics. The CeO_2–La_2O_3 NC exhibited superior degradation efficiency, achieving 93% under UV and 96.66% under solar irradiation within 180 minutes—significantly outperforming individual CeO_2 and La_2O_3 nanoparticles. These findings highlight the synergistic effect of the bimetallic system for efficient dye degradation applications.

REFERENCES

1. Manikandan V, Jayanthi P, Priyadharsan A, Vijayaprathap E, Anbarasan PM, Velmurugan P. Green synthesis of pH-responsive Al2O3 nanoparticles: Application to rapid removal of nitrate ions with enhanced antibacterial activity. Journal of Photochemistry and Photobiology A: Chemistry [Internet]. 2019;371:205–15. Available from: https://www.sciencedirect.com/science/article/pii/S1010603018312802
2. Kumar M, Rahman A, Singh VP. An efficient p-n type based (NiO/CeO2) hybrid composite photocatalyst and its performance for cationic dye degradation: Probable degradation pathways, optimization activities, and depth mechanism insights. Next Energy [Internet]. 2025;7:100228. Available from: https://www.sciencedirect.com/science/article/pii/S2949821X24001339
3. Chan SHS, Wu TY, Juan JC, Teh CY. Recent developments of metal oxide semiconductors as photocatalysts in advanced oxidation processes (AOPs) for treatment of dye waste-water. Journal of Chemical Technology and Biotechnology. 2011;86(9):1130–58.

4. Sauvé S, Desrosiers M. A review of what is an emerging contaminant. Chemistry Central Journal [Internet]. 2014;8(1):15. Available from: https://doi.org/10.1186/1752-153X-8-15
5. Saeed M, Muneer M, Haq A ul, Akram N. Photocatalysis: an effective tool for photodegradation of dyes—a review. Environmental Science and Pollution Research. 2022;29(1):293–311.
6. Singh K, Arora S. Removal of Synthetic Textile Dyes From Wastewaters: A Critical Review on Present Treatment Technologies. Critical Reviews in Environmental Science and Technology [Internet]. 2011 Apr 6;41(9):807–78. Available from: https://doi.org/10.1080/10643380903218376
7. Ahmad AL, Puasa SW. Reactive dyes decolourization from an aqueous solution by combined coagulation/micellar-enhanced ultrafiltration process. Chemical Engineering Journal [Internet]. 2007;132(1):257–65. Available from: https://www.sciencedirect.com/science/article/pii/S1385894707000113
8. Riera-Torres M, Gutiérrez-Bouzán C, Crespi M. Combination of coagulation–flocculation and nanofiltration techniques for dye removal and water reuse in textile effluents. Desalination [Internet]. 2010;252(1):53–9. Available from: https://www.sciencedirect.com/science/article/pii/S0011916409012776
9. Pandey B, Singh P, Kumar V. Photocatalytic-sorption processes for the removal of pollutants from wastewater using polymer metal oxide nanocomposites and associated environmental risks. Environmental Nanotechnology, Monitoring & Management [Internet]. 2021;16:100596. Available from: https://www.sciencedirect.com/science/article/pii/S2215153221001719
10. Kumari V, Kumar N, Yadav S, Mittal A, Sharma S. Novel mixed metal oxide (ZnO.La2O3.CeO2) synthesized via hydrothermal and solution combustion process - A comparative study and their photocatalytic properties. Materials Today: Proceedings [Internet]. 2019;19(xxxx):650–7. Available from: https://doi.org/10.1016/j.matpr.2019.07.748
11. Venkateshaiah A, Černík M, Padil VVT. Metal Oxide Nanoparticles for Environmental Remediation. In: Nanotechnology for Environmental Remediation [Internet]. Wiley; 2022. p. 183–213. Available from: https://doi.org/10.1002/9783527834143.ch11
12. Kavitha S, Jayamani N, Barathi D. Investigation on SnO2/TiO2 nanocomposites and their enhanced photocatalytic properties for the degradation of methylene blue under solar light irradiation. Bulletin of Materials Science [Internet]. 2021;44(1). Available from: https://doi.org/10.1007/s12034-020-02291-4
13. Xin Y, Wang Z, Qi Y, Zhang Z, Zhang S. Synthesis of rare earth (Pr, Nd, Sm, Eu and Gd) hydroxide and oxide nanorods (nanobundles) by a widely applicable precipitation route. Journal of Alloys and Compounds [Internet]. 2010;507(1):105–11. Available from: https://www.sciencedirect.com/science/article/pii/S0925838810018098
14. Iranmanesh T, Jahani S, Foroughi MM, Zandi MS, Hassani Nadiki H. Synthesis of La2O3/MWCNT nanocomposite as the sensing element for electrochemical determination of theophylline. Analytical Methods [Internet]. 2020;12(35):4319–26. Available from: http://dx.doi.org/10.1039/D0AY01336F
15. Kudo A, Miseki Y. Heterogeneous photocatalyst materials for water splitting. Chemical Society Reviews. 2009;38(1):253–78.
16. Tsai HC, Peng YH, Wen PY, Wu T, Lin YW. Enhanced visible light photocatalytic degradation of methylene blue by cds-zns-bipo4 nanocomposites prepared by a solvent-assisted heating method. Catalysts. 2021;11(9).
17. Dhall A, Self W. Cerium Oxide Nanoparticles: A Brief Review of Their Synthesis Methods and Biomedical Applications. Vol. 7, Antioxidants. 2018.
18. Younis A, Chu D, Li S. Cerium Oxide Nanostructures and their Applications. In: Farrukh MA, editor. Rijeka: IntechOpen; 2016. p. Ch. 3. Available from: https://doi.org/10.5772/65937
19. Madhu A, Eraiah B, Manasa P, Srinatha N. Nd3+-doped lanthanum lead boro-tellurite glass for lasing and amplification applications. Optical Materials [Internet]. 2018;75:357–66. Available from: https://www.sciencedirect.com/science/article/pii/S0925346717306705
20. Teo S, Guo Z, Xu Z, Zhang C, Kamata Y, Hayase S, et al. The Role of Lanthanum in a Nickel Oxide-Based Inverted Perovskite Solar Cell for Efficiency and Stability Improvement. ChemSusChem [Internet]. 2019 Jan 24;12(2):518–26. Available from: https://doi.org/10.1002/cssc.201802231

21. Meng W, Hu R, Yang J, Du Y, Li J, Wang H. Influence of lanthanum-doping on photocatalytic properties of BiFeO3 for phenol degradation. Chinese Journal of Catalysis [Internet]. 2016;37(8):1283–92. Available from: https://www.sciencedirect.com/science/article/pii/S187220671662449X
22. Mogha NK, Gosain S, Masram DT. Lanthanum oxide nanoparticles immobilized reduced graphene oxide polymer brush nanohybrid for environmental vitiation of organic dyes. Arabian Journal of Chemistry [Internet]. 2020;13(1):1367–76. Available from: https://www.sciencedirect.com/science/article/pii/S1878535217302162
23. Kumar M, Rahman A. Facile Synthesis, Characterization, and Photocatalytic study of La2O3/SnO2 Nanocomposites. Journal of The Institution of Engineers (India): Series E [Internet]. 2023 Jun 18;104(1):95–108. Available from: https://link.springer.com/10.1007/s40034-023-00267-7
24. Salavati-niasari M, Hosseinzadeh G, Davar F. Synthesis of lanthanum carbonate nanoparticles via sonochemical method for preparation of lanthanum hydroxide and lanthanum oxide nanoparticles. Journal of Alloys and Compounds [Internet]. 2011;509(1):134–40. Available from: http://dx.doi.org/10.1016/j.jallcom.2010.09.006
25. Mazloumi M, Zanganeh S, Kajbafvala A, Shayegh MR, Sadrnezhaad SK. Formation of Lanthanum hydroxide nanostructures: effect of NaOH and KOH solvents. International Journal of Engineering, Transactions B: Applications. 2008;21(2):169–76.
26. Kumar PR, Maharajan TM, Chinnasamy M, Prabu AP, Suthagar JA, Kumar KS. Hydroxyl radical scavenging activity of La2O3 nanoparticles. J Pharm Innov. 2019;8(5):759–763.
27. Farahmandjou M, Farahmandjou M, Zarinkamar M, Firoozabadi TP. Synthesis of Cerium Oxide (CeO2) nanoparticles using simple CO-precipitation method Article in Revista Mexicana de Fisica · Synthesis of Cerium Oxide (CeO 2) nanoparticles using simple CO-precipitation method. Revista Mexicana de Física [Internet]. 2016;62(October):496–9. Available from: https://www.researchgate.net/publication/308742876
28. Tumkur PP, Gunasekaran NK, Lamani BR, Nazario Bayon N, Prabhakaran K, Hall JC, et al. Cerium Oxide Nanoparticles: Synthesis and Characterization for Biosafe Applications. Nanomanufacturing. 2021;1(3):176–89.
29. Wen XJ, Niu CG, Zhang L, Liang C, Zeng GM. A novel Ag2O/CeO2 heterojunction photocatalysts for photocatalytic degradation of enrofloxacin: possible degradation pathways, mineralization activity and an in depth mechanism insight. Applied Catalysis B: Environmental [Internet]. 2018;221(July):701–14. Available from: http://dx.doi.org/10.1016/j.apcatb.2017.09.060
30. Kabir H, Nandyala SH, Rahman MM, Kabir MA, Stamboulis A. Influence of calcination on the sol–gel synthesis of lanthanum oxide nanoparticles. Applied Physics A: Materials Science and Processing [Internet]. 2018;124(12):1–11. Available from: http://dx.doi.org/10.1007/s00339-018-2246-5
31. Deus RC, Cortés JA, Ramirez MA, Ponce MA, Andres J, Rocha LSR, et al. Photoluminescence properties of cerium oxide nanoparticles as a function of lanthanum content. Materials Research Bulletin [Internet]. 2015;70:416–23. Available from: http://dx.doi.org/10.1016/j.materresbull.2015.05.006
32. Muchuweni E, Sathiaraj TS, Nyakotyo H. Synthesis and characterization of zinc oxide thin films for optoelectronic applications. Heliyon [Internet]. 2017;3(4):e00285. Available from: http://dx.doi.org/10.1016/j.heliyon.2017.e00285
33. Hafaiedh A, Bouarissa N. Quantum confinement effects on energy gaps and electron and hole effective masses of quantum well AlN. Physica E: Low-dimensional Systems and Nanostructures [Internet]. 2011;43(9):1638–41. Available from: https://www.sciencedirect.com/science/article/pii/S1386947711001718
34. Manuscript A. Dalton transactions. Journal of the Chemical Society, Dalton Transactions. 1972;1772.
35. Maria Magdalane C, Kaviyarasu K, Matinise N, Mayedwa N, Mongwaketsi N, Letsholathebe D, et al. Evaluation on La2O3 garlanded ceria heterostructured binary metal oxide nanoplates for UV/ visible light induced removal of organic dye from urban wastewater. South African Journal of Chemical Engineering [Internet]. 2018;26(July):49–60. Available from: https://doi.org/10.1016/j.sajce.2018.09.003

36. Petrucci RH. Genereal Chemistry. Principles and Modern Applications 9th ed New Jersey: Pearson Education Inc. 2007;
37. Liu IT, Hon MH, Teoh LG. The preparation, characterization and photocatalytic activity of radical-shaped CeO2/ZnO microstructures. Ceramics International [Internet]. 2014;40(3):4019–24. Available from: http://dx.doi.org/10.1016/j.ceramint.2013.08.053
38. Kumar M, Rahman A. Journal of Photochemistry & Photobiology , A : Chemistry Investigating the structural , optical , electrochemical , and photocatalytic properties of Lanthanum-Modified SnO 2 hybrid nanoparticles. Journal of Photochemistry & Photobiology, A: Chemistry [Internet]. 2024;452(December 2023):115553. Available from: https://doi.org/10.1016/j.jphotochem.2024.115553
39. Hemalatha P, Karthick SN, Hemalatha K V., Yi M, Kim HJ, Alagar M. La-doped ZnO nanoflower as photocatalyst for methylene blue dye degradation under UV irradiation. Journal of Materials Science: Materials in Electronics. 2016;27(3):2367–78.
40. Li H, Feng B. Visible-light-driven composite La2O3/TiO2 nanotube arrays: Synthesis and improved photocatalytic activity. Materials Science in Semiconductor Processing [Internet]. 2016;43:55–9. Available from: http://dx.doi.org/10.1016/j.mssp.2015.11.021
41. Bomila R, Srinivasan S, Gunasekaran S, Manikandan A. Enhanced photocatalytic degradation of methylene blue dye, opto-magnetic and antibacterial behaviour of pure and la-doped ZnO nanoparticles. Journal of Superconductivity and Novel Magnetism. 2018;31(3):855–64.
42. Sudhagar S, Kumar SS, Premkumar IJI, Vijayan V, Venkatesh R, Rajkumar S, et al. UV- and visible-light-driven TiO2/La2O3 and TiO2/Al2O3 nanocatalysts: synthesis and enhanced photocatalytic activity. Applied Physics A: Materials Science and Processing. 2022;128(4).
43. Fazil AA, Narayanan S, Begum MS, Manikandan G, Yuvashree M. Green synthesis strategy for producing doped and undoped ZnO nanoparticles: their photocatalytic studies for industrial dye degradation. Water Science and Technology. 2021;84(10–11):2958–67.
44. Reza KM, Kurny A, Gulshan F. Parameters affecting the photocatalytic degradation of dyes using TiO2: a review. Applied Water Science. 2017;7(4):1569–78.
45. Madkour M, Allam OG, Abdel Nazeer A, Amin MO, Al-Hetlani E. CeO2-based nanoheterostructures with p–n and n–n heterojunction arrangements for enhancing the solar-driven photodegradation of rhodamine 6G dye. Journal of Materials Science: Materials in Electronics [Internet]. 2019;30(11):10857–66. Available from: https://doi.org/10.1007/s10854-019-01429-3
46. Hasnat MA, Siddiquey IA, Nuruddin A. Comparative photocatalytic studies of degradation of a cationic and an anionic dye. Dyes and Pigments [Internet]. 2005;66(3):185–8. Available from: https://www.sciencedirect.com/science/article/pii/S0143720804002438
47. Makofane A, Motaung DE, Hintsho-Mbita NC. Photocatalytic degradation of methylene blue and sulfisoxazole from water using biosynthesized zinc ferrite nanoparticles. Ceramics International [Internet]. 2021;47(16):22615–26. Available from: https://doi.org/10.1016/j.ceramint.2021.04.274
48. Wang S, Bai L, Ao X. Preparation and photocatalytic application of a S, Nd double doped nano-TiO 2 photocatalyst. RSC Advances [Internet]. 2018;8(64):36745–53. Available from: https://xlink.rsc.org/?DOI=C8RA06778C
49. Shukla S, Pandey H, Singh P, Tiwari AK, Baranwal V, Pandey AC. Synergistic impact of photocatalyst and dopants on pharmaceutical-polluted waste water treatment: a review. Environmental Pollutants and Bioavailability [Internet]. 2021;33(1):347–64. Available from: https://doi.org/10.1080/26395940.2021.1987843
50. Xu Y, Schoonen MAA. The absolute energy positions of conduction and valence bands of selected semiconducting minerals. American Mineralogist [Internet]. 2000 Mar;85(3–4):543–56. Available from: https://www.degruyter.com/document/doi/10.2138/am-2000-0416/html
51. Kusmierek E. A CeO2 semiconductor as a photocatalytic and photoelectrocatalytic material for the remediation of pollutants in industrial wastewater: A review. Catalysts. 2020;10(12):1–54.

